Estimating near-surface specific humidity over convective oceanic regions from cloud base height observations

Anna Lea Albright[1], Bjorn Stevens[2], and Martin Wirth[3]

[1]Harvard University Department of Earth and Planetary Sciences, Cambridge, MA, 02138, USA
[2]Max Planck Institute for Meteorology, 20255 Hamburg, Germany
[3]Institut für Physik der Atmosphäre, Deutsches Zentrum für Luft- und Raumfahrt (DLR), Oberpfaffenhofen, 82234 Wessling, Germany

Correspondence: Anna Lea Albright (annaleaalbright@fas.harvard.edu)

Abstract.

The surface moisture flux is a large term in the surface energy balance and difficult to estimate remotely. The main difficulty for its remote estimation is a poor ability to measure near-surface humidity. Current methods to retrieve near-surface specific humidity approach the problem statistically and have errors of approximately $1\,\mathrm{g\,kg^{-1}}$ even in global, annual averages. Using extensive measurements from the EUREC[4]A field campaign (ElUcidating the RolE of Clouds, Circulation Coupling in Climate), we demonstrate that remote sensing measurements of cloud base height can provide useful estimates of near-surface humidity over convective oceanic regions where optically-thick clouds do not prevent lidar sampling. First applying the method to 171 coincident radiosonde and ceilometer pairings collected from a research vessel from January 18 to February 14, 2020 yields skillful predictions of near-surface specific humidity regarding the mean (mean bias $0.33\,\mathrm{g\,kg^{-1}}$ compared to observed) and its variability ($r = 0.76$). We then apply this method using an airborne lidar to estimate cloud base height from above. In two representative case studies, we find similar skill in the predicted humidity, with low mean biases (-0.06 and $-0.03\,\mathrm{g\,kg^{-1}}$ compared to observed) with substantial variability captured ($r = 0.61$ and $r = 0.57$, respectively). Besides estimates of cloud base height, we highlight two main error sources: (i) the relative humidity lapse rate below cloud base and (ii) the temperature difference between the sea surface and near-surface air, which would need to be calibrated if using this method to develop an operational product to estimate the near-surface specific humidity from downward-looking spaceborne lidar. This proof of concept raises the potential for application over convective oceanic regions where lidar sampling of cloud base is possible. This method could provide a physics-based augmentation to existing, more empirical approaches and therefore provide an additional observational constraint on the surface energy budget.

1 Introduction

The surface energy balance is a fundamental property of the climate system. How it is partitioned among its different components, and how it varies in space and time tempers the behavior of the atmosphere above, and the land or water below (e.g., Hartmann, 2015). Among its varied components, the main balance is between moisture fluxes, extracting energy from the surface through evaporation, and the absorption of energy from the sun. Sensible energy transfers, and net radiant energy fluxes

in the thermal infrared also combine to cool the surface, but on average only half as strongly as the evaporation of water which
25 maintains the flux of moisture to the atmosphere (e.g., Hartmann, 2015). In addition to providing an energetic link between
the surface and the atmosphere, the moisture flux links the water and the energy cycles (e.g., Jackson et al., 2009; Kubota and
Tsutomu, 2008; Fajber et al., 2023). Despite their importance, the evaporative (or moisture) fluxes are difficult to measure, and
they are both one of the largest, and most uncertain terms in the surface energy balance (e.g., Liman et al., 2018; Clayson et al.,
2019). An improved ability to quantify evaporative fluxes is therefore essential for observation-based studies of the water and
30 energy cycles, and the dynamics of weather systems and circulations that they fuel.

These fluxes can be reasonably well estimated from the covariance of anomalies in moisture, q', and vertical air motions,
w', i.e., as $\rho\ell_v\overline{w'q'}$, with ρ the density and ℓ_v the vaporization enthalpy. Surface layer similarity provides a mean field theory
for the evaporative flux, which is encapsulated by the bulk aerodynamic formula (e.g., Fairall et al., 1996b, 2003; Edson et al.,
2013), taking the form,

$$35 \quad \overline{w'q'} = C|U|\Delta q, \quad \text{where} \quad \Delta q \equiv q_s - q_a \tag{1}$$

so that the evaporative flux can be directly related to the difference, Δq, in the specific humidity deficit of the air, q_a, as
compared to the surface, q_s, and the near-surface wind speed, $|U|$, with C being an exchange coefficient. The value of C can
depend on the surface properties and stability in a complex way, but it is well characterized by decades of careful measurements
calibrating theoretical expectations (Fairall et al., 1996b, 2003; Edson et al., 2013). The surface moisture fluxes can therefore
40 be reasonably well determined given knowledge of the specific humidity of the near-surface air, q_a, the saturation specific
humidity at the surface temperature and pressure, q_s, as well as the near-surface winds, $|U|$.

Following the bulk aerodynamic formulation of surface fluxes, we assume that the water vapor pressure at the ocean surface
is at saturation, so that the surface specific humidity q_s equals the saturation specific humidity $q_*(T_s, P_s)$. This approximation
in bulk theory reflects the near-equilibrium condition at the air–sea interface and is a standard assumption in flux parameter-
45 izations, sometimes with a 0.98 correction for typical salinity (e.g., Fairall et al., 1996b, 2003). Satellite remote sensing can
provide reasonable estimates of T_s, which given P_s determines q_* and hence q_s. Likewise a variety of measurements provide
increasingly accurate estimates of surface wind speeds (e.g., Ricciardulli and Manaster, 2021). The main limitation in esti-
mating evaporative fluxes over the ocean is therefore the measurement of the near-surface specific humidity of the air, q_a, a
quantity for which there is no real proxy. As a result, satellite-based climatologies of evaporative fluxes over the ocean depend
50 on q_a correlating with other quantities that can be remotely sensed, so that it (or the evaporative flux as a whole) can be in-
ferred statistically. Gentemann et al. (2020) detail approaches to this problem. These include retrievals from passive microwave
measurements, such as the Hamburg Ocean Atmosphere Parameters and Fluxes from Satellite (HOAPS4) (Liman et al., 2018;
Andersson et al., 2010) and SeaFlux CDR (Clayson and Brown, 2016), as well as approaches that combine reanalysis and
passive microwave data, such as IFREMER4 (Bentamy et al., 2013, 2017a) and J-OFURO3 (Tomita et al., 2019). Liman et al.
55 (2018), for instance, compared HOAPS climatology with *in situ* buoy and ship measurements and found retrieval uncertainties
in latent heat flux of $15\,\mathrm{W\,m^{-2}}$, with a global-mean error of 25 Wm^{-2}. Errors were found to be particularly large over the

subtropical oceans, where evaporative fluxes are large in magnitude, with an average of 37 Wm^{-2} in random instantaneous retrieval errors (Liman et al., 2018).

A number of studies have confirmed that the most uncertain term in Eq. 1 is q_a (e.g., Bourras, 2006; Tomita and Kubota, 2006; Jackson et al., 2009; Bentamy et al., 2017b; Roberts et al., 2019; Robertson et al., 2020). Liman et al. (2018) estimated that contributions from q_a contribute approximately 60% to overall uncertainty in the evaporative flux, whereas uncertainties from the wind speed contribute about 25%.

Given this uncertainty, our goal is to develop a method to estimate q_a over convective oceanic regions. To this end, we exploit the physical connection between cloud base height h and near-surface relative humidity W_a: in a convective, well-mixed subcloud layer the cloud base forms near the lifting condensation level (LCL) and thus the height at which it forms depends primarily on near-surface T and q.

Our method takes advantage of the fact that a convective cloud-topped boundary layer is ubiquitous over the world oceans (Fig. 1). We demonstrate this ubiquity by analyzing daily ERA5 surface fluxes from the year 2020 to compute the climatological frequency of positive surface buoyancy flux, B_0, representing the annual frequency of convectively unstable surface conditions. The resulting 'buoyancy-favorability' map (Fig. 1) shows that near-surface convective instability prevails over most tropical and subtropical oceans, with ocean-only mean frequencies of 85% globally and 99% between 30° S and 30° N.

Building on this link, we test the idea that W_a (and hence q_a) can be inferred from h and a small set of parameters, as a basis for a possible retrieval. To this end, we summarize notation and data (Sec. 2); we then derive the relationship between h, W_a, and $\Delta q \equiv q_s - q_a$ and quantify sources of uncertainty (Sec. 3). Using coincident ceilometer–radiosonde and lidar–dropsonde measurements from EUREC^{4}A, we validate the h–W_a linkage from surface and airborne platforms (Sec. 4.1, 4.2). We estimate the two near-surface control parameters, $\mathrm{d}W/\mathrm{d}z$ and $\Delta_a T$, from observations (Sec. 4.3) and evaluate retrieval skill in q_a (Sec. 4.4). Finally, we discuss scope, caveats, and practical use, and conclude (Sec. 5, 6).

2 Notation and data

Throughout, for notation, the subscript s denotes surface quantities and the subscript a denotes near-surface atmospheric quantities evaluated at the reference height $z_a = 40\,\mathrm{m}$. This height corresponds to the lowest reliable sonde level and is close to the R/V Meteor air-temperature measurements at $28.3\,\mathrm{m}$ used in this study. The ocean surface temperature T_s is the skin temperature. Near-surface atmospheric variables carry the a subscript; for example, q_a, T_a, and W_a refer to conditions at z_a. Air pressure is denoted by P and vapor pressure by e, with e_* denoting the saturation value for a plane of pure water. Hence, because the surface is water (albeit wavy and not pure), $e_s \approx e_*(T_s)$. To make it easier to manipulate in equations, for which abbreviations make poor symbols, we use the symbol W to denote relative humidity.

Regarding data, we employ coincident sounding and lidar data from ground-based and airborne observing platforms during the EUREC^{4}A field campaign (ElUcidating the RolE of Clouds, Circulation Coupling in Climate), which took place in January and February 2020 in the trade-wind zone east of Barbados (Bony et al., 2017; Stevens et al., 2021; Albright et al., 2022). During EUREC^{4}A the German High Altitude and Long Range Research Aircraft (HALO) launched 810 dropsondes between
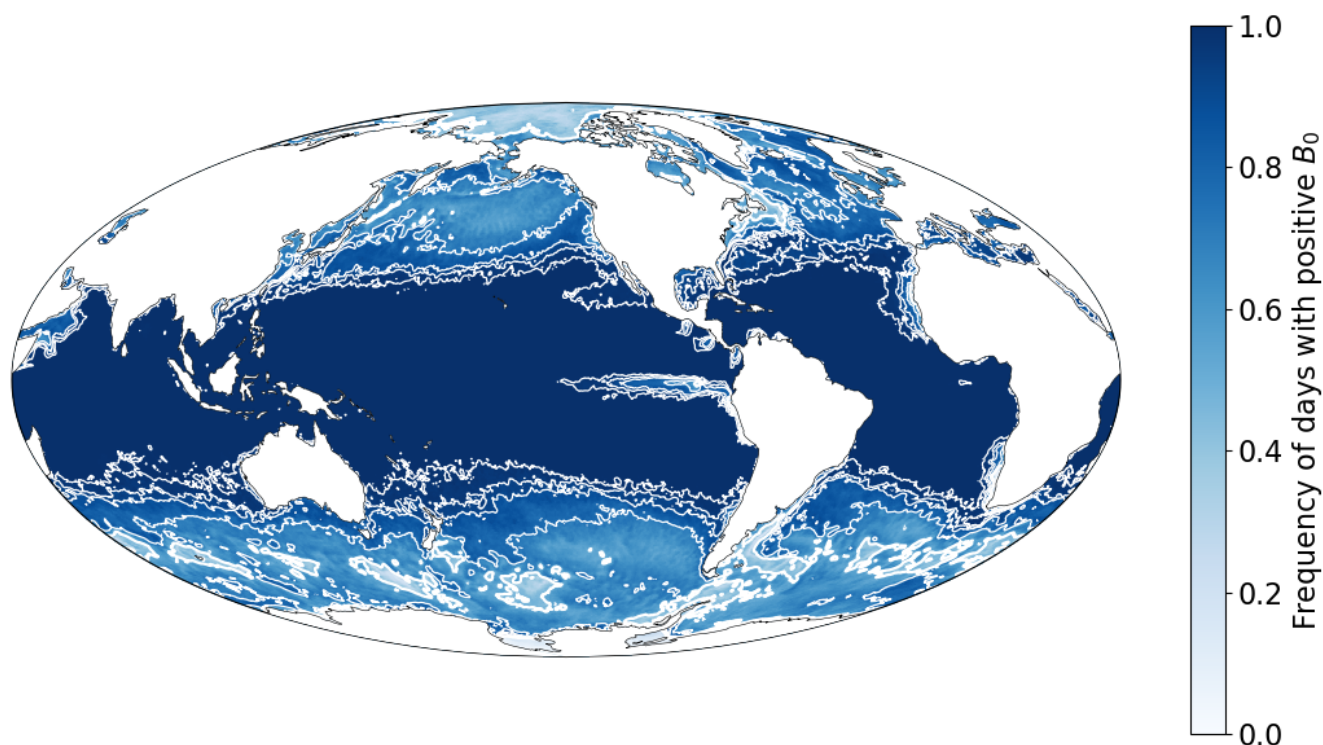
Figure 1. Frequency of days with positive surface buoyancy flux, B_0, during 2020, computed from daily ERA5 reanalysis data of sensible and latent heat fluxes, as well as the 2 m air temperature. The shading indicates the fraction of days for which the surface buoyancy flux is positive (upward). Positive values represent convectively unstable surface conditions. Values approach unity over most tropical and subtropical ocean regions, indicating nearly continuous convective instability. Over the global oceans, the area-weighted mean frequency is approximately 85%, while in the tropical band (30° S–30° N) it reaches 99%. White contours denote frequencies of 0.50, 0.75, 0.90, 0.95, and 0.99.

90 January 22, 2020 and February 15, 2020 (George et al., 2021) (see the EUREC⁴A data paper for HALO by Konow et al. (2021)). These dropsondes yield vertical profiles of pressure, temperature, and relative humidity with a manufacturer-stated accuracy of 0.4 hPa, 0.1°C, and 2%, respectively (Vaisala, 2020). During EUREC⁴A, dropsonde measurements were distributed along a fixed flight pattern, the 'EUREC⁴A circle' — a circular flight pattern with an approximately 220-kilometer diameter, centered at 13.3°N, 57.7°W, at 9.5 km altitude. Following Bony et al. (2017); Stevens et al. (2021), one *circle-mean* refers to the mean
95 of typically 12 dropsondes launched over one hour along the EUREC⁴A circle (due to operator and instrument errors, on some circles fewer sondes were launched, but never fewer than seven). A *circling-mean* is defined as the mean of three consecutive circle-means, corresponding to 30–36 consecutive soundings aggregated over 210 minutes (see Albright et al. (2022) and Vogel et al. (2022) for further information). This sampling strategy provides aggregated, statistical estimates of a large-scale signal.

   Also onboard the HALO aircraft, the airborne demonstrator for the WAter vapor Lidar Experiment in Space (WALES)
100 measured atmospheric backscatter and water vapor DIfferential Absorption Lidar (DIAL) profiles (Wirth et al., 2009; Konow

et al., 2021). Due to its high horizontal and vertical resolution, airborne lidar data is amenable to studying small-scale clouds, such as in trade cumulus regions. Here we evaluate the lidar data at the highest possible resolution, e.g., the backscatter ratio and aerosol depolarization data are analyzed at 0.2 second time resolution and 7.5 m vertical resolution. For the analyzed flights, the altitude was nearly constant (10.4 km) and the aircraft speed was about 210 m/s, resulting in consistent horizontal

105   spatial resolution of 42 m (Konow et al., 2021). We use data at a wavelength of 532 nm, and the backscatter profiles are extinction corrected using the High Spectral Resolution Lidar (HSRL) method (Esselborn et al., 2008). All data are regridded to a constant altitude scale over the EGM96 geoid.

    Over the same time period, radiosondes were launched as part of the campaign from the Barbados Cloud Observatory (BCO, Stevens et al., 2016) and the research vessel, R/V Meteor (Stephan et al., 2020), from January 16 to March 1, 2020. As described

110   in Stevens et al. (2021), ceilometer measurements of cloud base height were made from January 18, 2020 to February 14, 2020 from the same platforms. At the BCO, the ceilometer is an OTT CHM 15k pulsed laser cloud height detector at 1064 nm used to detect cloud base height and lifting condensation level; at the R/V Meteor, the ceilometer is a Jenoptik system measuring vertical profiles of attenuated backscatter at 1064 nm to infer cloud base as a function of altitude and aerosol (Stevens et al., 2021).

115   **3   Theory and parameter sensitivities for cloud base height as a proxy for near-surface humidity**

Before quantifying empirical relationships between cloud base height, h, and near-surface relative humidity (W_{a}), we outline the theoretical basis linking both quantities. In a well-mixed and unsaturated subcloud layer, the specific humidity is nearly constant while temperature follows a dry-adiabatic profile. Relative humidity is defined as

$$W = \frac{e}{e_*(T)} = q\frac{R_{\mathrm{v}}}{R}\frac{P}{e_*(T)}, \tag{2}$$

120   where $R = (1-q)R_{\mathrm{d}} + qR_{\mathrm{v}}$ is the gas constant of an ideal mixture of 'dry-air' and water vapor, $e_*(T)$ is the saturation vapor pressure, and q the specific humidity.

    For an adiabatic process for which pressure varies hydrostatically, $\mathrm{d}T/\mathrm{d}z = -g/c_p$, and negligible vertical humidity gradients ($\mathrm{d}q/\mathrm{d}z \approx 0$), the vertical gradient of W simplifies to

$$\frac{\mathrm{d}W}{\mathrm{d}z} = \frac{g}{T}\left(\frac{\ell_{\mathrm{v}}}{c_p R_{\mathrm{v}} T} - \frac{1}{R}\right)W, \tag{3}$$

125   which gives the adiabatic rate of increase of relative humidity with height. Averaging across a well-mixed boundary layer with a depth of 600 m, $q = 15\,\mathrm{g\,kg^{-1}}$ and T varying dry-adiabatically about a mid-layer (300 m) mean value of 296.41 K – values derived from the Meteor and BCO radiosondes – yields a boundary layer mean value of $\frac{\mathrm{d}W}{\mathrm{d}z} = 4.0\,\%\,\mathrm{hm^{-1}}$ (referring to percent per hectometer, or 100 m).

    In reality, the subcloud layer departs slightly from adiabaticity due to entrainment of drier air from above and the partial

130   compensation of temperature and moisture tendencies by turbulent mixing (Wyngaard and Brost, 1984). Allowing weak vertical

gradients in both T and q, the more general form of the relative-humidity lapse rate is

$$\frac{\mathrm{d}W}{\mathrm{d}z} = \left[\left(\frac{1}{q} - \frac{R_\mathrm{v} - R_\mathrm{d}}{R}\right)\frac{\mathrm{d}q}{\mathrm{d}z} - \frac{g}{RT} - \frac{\ell_\mathrm{v}}{R_\mathrm{v}T^2}\frac{\mathrm{d}T}{\mathrm{d}z}\right]W, \tag{4}$$

which reduces to Eq. (3) when $\mathrm{d}q/\mathrm{d}z = 0$ and $\mathrm{d}T/\mathrm{d}z = -g/c_p$.

Using representative trade-wind conditions from Albright et al. (2022), $\mathrm{d}q/\mathrm{d}z \approx -1\,\mathrm{g\,kg^{-1}\,km^{-1}}$ and $\mathrm{d}T/\mathrm{d}z \approx -9.4\,\mathrm{K\,km^{-1}}$,

135 together with $T = 296.4\,\mathrm{K}$ and $q = 15\,\mathrm{g\,kg^{-1}}$, Eq. (4) gives $\left(\frac{1}{W}\right)\frac{\mathrm{d}W}{\mathrm{d}z} \approx 4.0 \times 10^{-4}\,\mathrm{m^{-1}}$, corresponding to $\frac{\mathrm{d}W}{\mathrm{d}z} \approx 3.6\,\%\,\mathrm{hm^{-1}}$ for $W \simeq 0.9$. This non–well-mixed estimate is about 10% smaller than the adiabatic value, with most of the reduction arising from the moisture-dilution term $\left(\frac{1}{q} - \frac{R_\mathrm{v}-R_\mathrm{d}}{R}\right)\frac{\mathrm{d}q}{\mathrm{d}z}$.

3.1 From relative to specific humidity

Given a cloud base at height h, where $W = 100\%$, the relative humidity at a reference height z_a below cloud base can be

140 approximated as

$$W_\mathrm{a} \approx 1 - (h - z_\mathrm{a})\frac{\mathrm{d}W}{\mathrm{d}z}. \tag{5}$$

From Eq. (2), the near-surface specific humidity deficit, $\Delta q = q_\mathrm{s} - q_\mathrm{a}$, may then be written as

$$\Delta q = q_\mathrm{s}\left\{1 - W_\mathrm{a}\left[\frac{e_*(T_\mathrm{a})}{e_*(T_\mathrm{s})}\right]\frac{P_\mathrm{s} - [1 - R_\mathrm{d}/R_\mathrm{v}]e_*(T_\mathrm{s})}{P_\mathrm{a} - [1 - R_\mathrm{d}/R_\mathrm{v}]W_\mathrm{a}e_*(T_\mathrm{a})}\right\}. \tag{6}$$

Linearizing $e_*(T)$ about T_s using the Clausius–Clapeyron relation,

145 $$e_*(T_\mathrm{a}) \approx e_*(T_\mathrm{s})\left[1 - \chi\,\Delta_a T\right], \qquad \chi = \frac{\ell_\mathrm{v}}{R_\mathrm{v}T_\mathrm{s}^2} \approx 1/16\ \mathrm{K^{-1}}, \tag{7}$$

and neglecting small pressure effects simplifies Eq. (6) to

$$\Delta q \approx q_\mathrm{s}\left[1 - W_\mathrm{a} + \chi\,\Delta_a T\,W_\mathrm{a}\right], \tag{8}$$

where $\Delta_a T = T_\mathrm{s} - T_\mathrm{a}$ is the sea–air temperature difference. Substituting Eq. (5) links Δq explicitly to h, the vertical gradient $\mathrm{d}W/\mathrm{d}z$, and $\Delta_a T$.

150 The corresponding fractional uncertainty in Δq from errors in h and $\Delta_a T$ (first-order propagation) is

$$\varepsilon_q \approx W_\mathrm{a}\varepsilon_h + \frac{\chi\,\Delta_a T\,W_\mathrm{a}}{1 - (1 - \chi\,\Delta_a T)W_\mathrm{a}}\,(\varepsilon_h + \varepsilon_T), \tag{9}$$

where $\varepsilon_h \equiv \delta\big[h\,(\mathrm{d}W/\mathrm{d}z)\big]/\big[h\,(\mathrm{d}W/\mathrm{d}z)\big]$ and $\varepsilon_T \equiv \delta(\Delta_a T)/\Delta_a T$ are fractional errors, and W_a is used as a fraction. For typical values $W_\mathrm{a} = 0.90$, $\Delta_a T = 1.3\,\mathrm{K}$, and $\chi \approx 1/16\ \mathrm{K^{-1}}$,

$$\varepsilon_q \approx 1.32\,\varepsilon_h + 0.42\,\varepsilon_T.$$

155 This analysis reinforces Eq. (9): the dominant source of uncertainty in Δq is the estimate of the product of h and $\mathrm{d}W/\mathrm{d}z$. Errors in the air–sea temperature contrast, $\Delta_a T$, also propagate into the energy budget via the sensible heat flux, producing same-sign errors in the net surface energy flux. The resulting fractional error scales with the Bowen ratio, B, as $(1 + 0.13/B)\,\varepsilon_T$,

growing as B decreases. For climatological oceanic conditions ($B \approx 0.1$) (Oliver, 2005), this amplification factor is ~ 2.3, which is still insufficient for ε_T to become comparable to the contribution from an equal ε_h.

Figure 2 summarizes these relationships schematically, showing how h, $\mathrm{d}W/\mathrm{d}z$, and $\Delta_a T$ combine to determine the near-surface specific humidity deficit Δq.
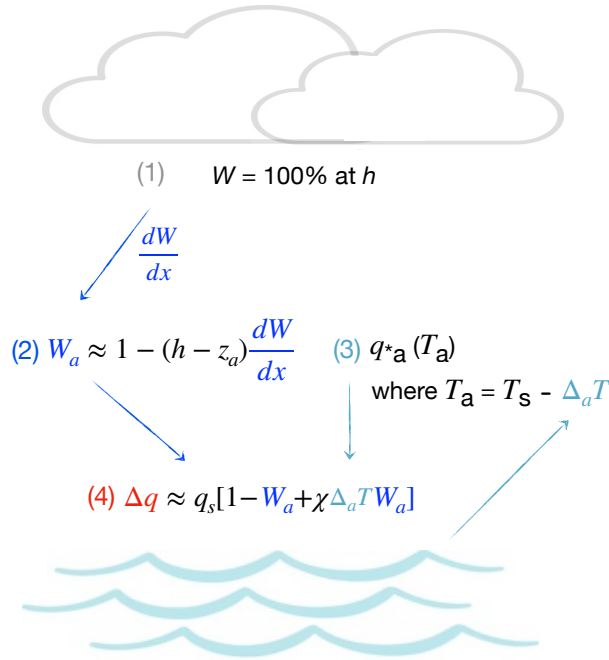

Figure 2. Schematic overview of the methodology highlighting the three main error sources: (1) estimating cloud base height, h, where $W = 100\%$ is assumed and then extrapolated to z_a using (2) a fixed relative humidity lapse rate $\frac{\mathrm{d}W}{\mathrm{d}z}$, which is then converted to q_a as described in the text with (3) a fixed $\Delta_\mathrm{a} T = 1.3\,\mathrm{K}$.

4 Results

4.1 Ground-Based Validation

For the ground-based validation, we use W from radiosondes and cloud base height distributions that are derived from ceilometer measurements during 60 minute windows centered on the radiosonde launch time. From the resulting distribution of ceilometer cloud detections, we associate h with the first and major peak of the distribution calculated from a Gaussian kernel density estimate, similar to the method employed in Albright et al. (2022) and Vogel et al. (2022). There is a strong correlation between h and the 10th percentile (r=0.94) or other low quantiles. Associating cloud base with the main peak of the distribution (or low quantiles) accounts for the expectation that ceilometer based cloud detections are skewed to more elevated

7
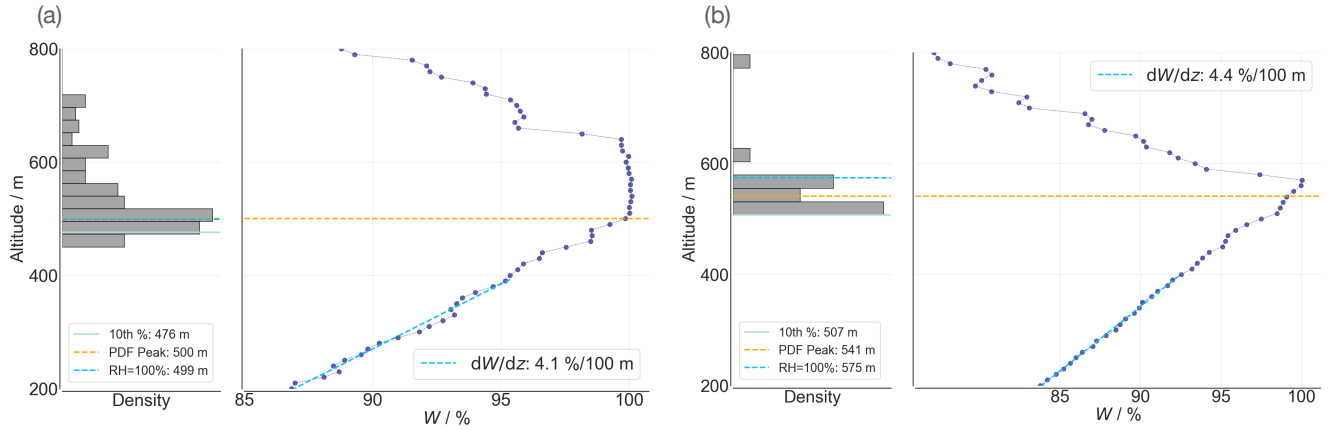
Figure 3. Ceilometer cloud returns for 30 minutes before and after the radiosonde launch time (grey histograms) and the relative humidity profiles measured by the radiosondes (blue profiles, data every 10 m). Also shown on the ceilometer cloud base height histograms are the 10th percentile (solid light blue line), the first major peak of the distribution calculated from a Gaussian kernel density estimate (orange dashed line), and the height at which relative humidity would reach 100% when extrapolating from a linear regression fit to the observed profile from 200-400 m (turquoise dashed line), as described in the text. Panel (a) is around the radiosonde launched on Jan. 29, 2020 at 06:44 UTC (2:44 am local Barbados time) and panel (b) is Feb. 1 2020 at 00:25 UTC (8:25 pm local Barbados time). These are two cases where radiosonde relative humidity reached 100% below 1000 m.

170   values (Nuijens et al., 2014). This skewness is expected from the tendency of clouds to evaporate from their base upwards, leaving cloud remnants to dissipate above cloud base. Similarly a local maximum in the wind speed near cloud base results in cloud base scudding ahead of more elevated regions of the cloud mass, which would also lead to a longer tail of more elevated ceilometer cloud returns. Rain, on the other hand, is infrequent and not readily identified in the ceilometer signal, leading less often to the situation whereby ceilometer estimates of h are low-biased (Nuijens et al., 2014). Fig. 3 illustrates this method for

175   two example 60 minute periods for radiosondes where relative humidity reached 100% below 1000 m. First ceilometer cloud detections are plotted as a histogram for the two cases, along with associated radiosonde profiles of relative humidity. For the ceilometer cloud base height distribution, horizontal lines illustrate different choices of h: the 10th percentile, first distribution peak, and the extrapolation to the altitude where W reaches 100% based on linear fits to W in the layer between 200-400 m.

    Using the first distribution peak of ceilometer values to estimate h, we calculate h and W_a for 118 radiosondes at the BCO

180   and 171 radiosondes at the R/V Meteor. Fig. 4 shows the close association between these two quantities. Also shown for comparison are subcloud layer height estimates from dropsonde measurements and virtual potential temperature, θ_v, vertical profiles (averaged at the $\sim$220 km diameter circle spatial scale, over three hours, following Vogel et al. (2022) and Albright et al. (2022)). Theoretical estimates from Eq. 4 are also plotted, both the adiabatic case and a case where $\frac{dT}{dz}$ departs from its adiabatic profile. The agreement between the lines and the points in Fig. 4 show the expected consistency.
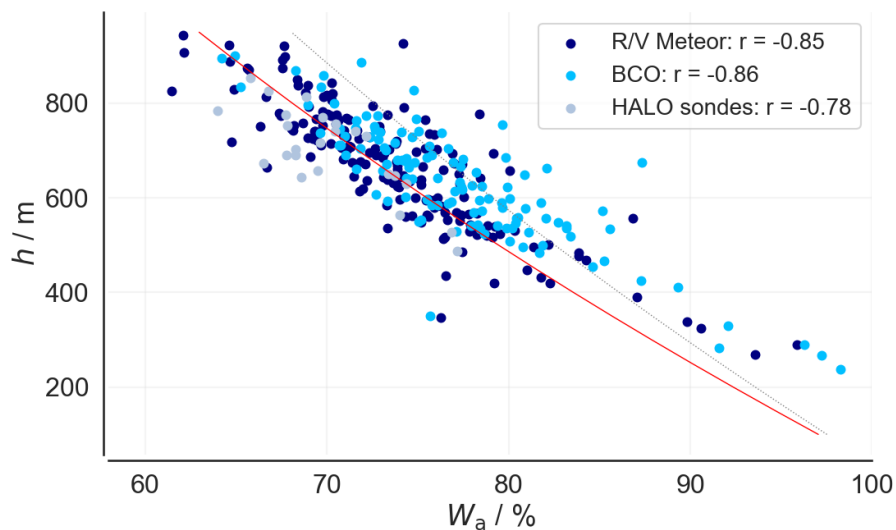
Figure 4. Near-surface relative humidity at $40\,\mathrm{m}$, W_a, from radiosondes and ceilometer-based estimates of cloud base height, h (using the first, major peak of the distribution) from R/V Meteor (n=171, dark blue) and BCO (n=118, medium blue) measurements. Also shown are area-averaged estimates of h from HALO dropsondes (light blue) as calculated by Vogel et al. (2022) and Albright et al. (2022). Lines are theoretical relationships as described in the text (red: adiabatic lapse rate of -9.8 K/km; light grey dashed line: temperature lapse rate of -8.5 K/km).

## 4.2 Testing the method with airborne lidar data

Having established the relationship between h and W_a based on both theory and surface measurements, we now turn to estimating the relationship using data from WALES airborne data. For each profile, the lowest altitude where the lidar signal is above background aerosol values is selected using a backscatter ratio of 20. The threshold for the backscatter ratio was set to 20 to ensure it lies well above values typically associated with strong aerosol loadings, which can reach up to around 10 for transported desert dust. Lowering the threshold would identify more clouds; however, the resulting change in relative humidity is minimal (about 1% when varying the threshold from 10 to 20) and becomes negligible (around 0.1%) when increasing it further from 20 to 40. We only consider cases where the sea surface is still visible, which ensures the accuracy of the extinction correction by the HSRL method. This consideration limits detections to optically-thin clouds or the corner regions of clouds, as deeper clouds are opaque to the downward-staring lidar, and has the advantage of being less susceptible to rain detections. For edge cases this implies that the cloud base near the edges of the clouds can be extrapolated to the center of the cloud, which is opaque to the lidar (e.g., assuming that the clouds are mostly flat at the bottom). For multi-layered cloud systems, the base of the upper layer is sometimes identified instead of the lowest cloud base. These cases could be flagged and removed based on a cloud base height histogram controlled filter which uses the fact that for multilayer systems a second or third mode appears. As discussed above in the case of surface-based measurements, 3D effects can also bias cloud bases high when the

200 cloud is vertically skewed by wind shear, a situation that Nuijens et al. (2014) showed was not uncommon for the winter trades near Barbados. Under those conditions, the lidar will only intersect the top cloud base region. We minimize these effects by applying a running minimum filter with a width of $3\,\mathrm{km}$.
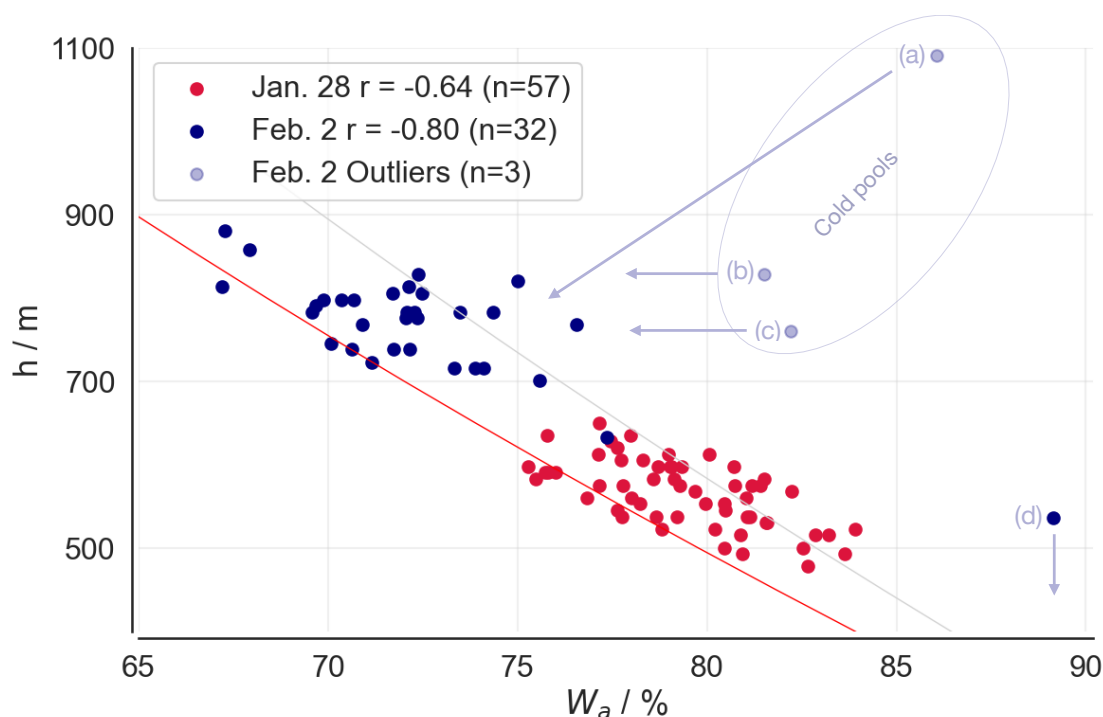
Figure 5. Cloud base height, h, from WALES for two days, January 28, 2020 (red) and February 2, 2020 (blue), and relative humidity at 40 m, W_{a}, from the nearest dropsonde launch. Outliers are labeled as (a), (b), (c), and (d), with the suspected source of bias discussed in the text and further illustrated in Fig. 6. As in Fig. 4, lines are theoretical relationships (red: adiabatic lapse rate of -9.8 K/km; light grey line: temperature lapse rate of -8.5 K/km).

Figure 5 presents results for two days of the campaign: January 28, 2020 (57 WALES lidar–dropsonde pairings) and February 2, 2020 (32 pairings), which are selected because they sampled a representative range of cloud base conditions.

205 January 28 was characterized by small cumulus clouds, often referred to as 'sugar' clouds (e.g., Stevens et al., 2020; Bony et al., 2020), while February 2 was characterized by deeper clouds with more stratiform layers near cloud top, referred to as 'flower' clouds (e.g., Stevens et al., 2020) and the presence of a strong Saharan dust layer reaching up to 2.5 km. Overall there is a good correspondence between h as measured by WALES and the dropsonde W_{a}, all the more so given that the W_{a} is a point estimate not necessarily centered on the lidar estimates.

210 A few outliers from the rest of the data are apparent in Fig. 5. An analysis of these exceptions helps give confidence in the rule, i.e., the purported $W_a(h)$ relation. For the February 2, 2020 case, which had more stratiform clouds, three outliers are identified. To investigate these outliers, we examine the backscatter data used to estimate the cloud base height, vertical profiles
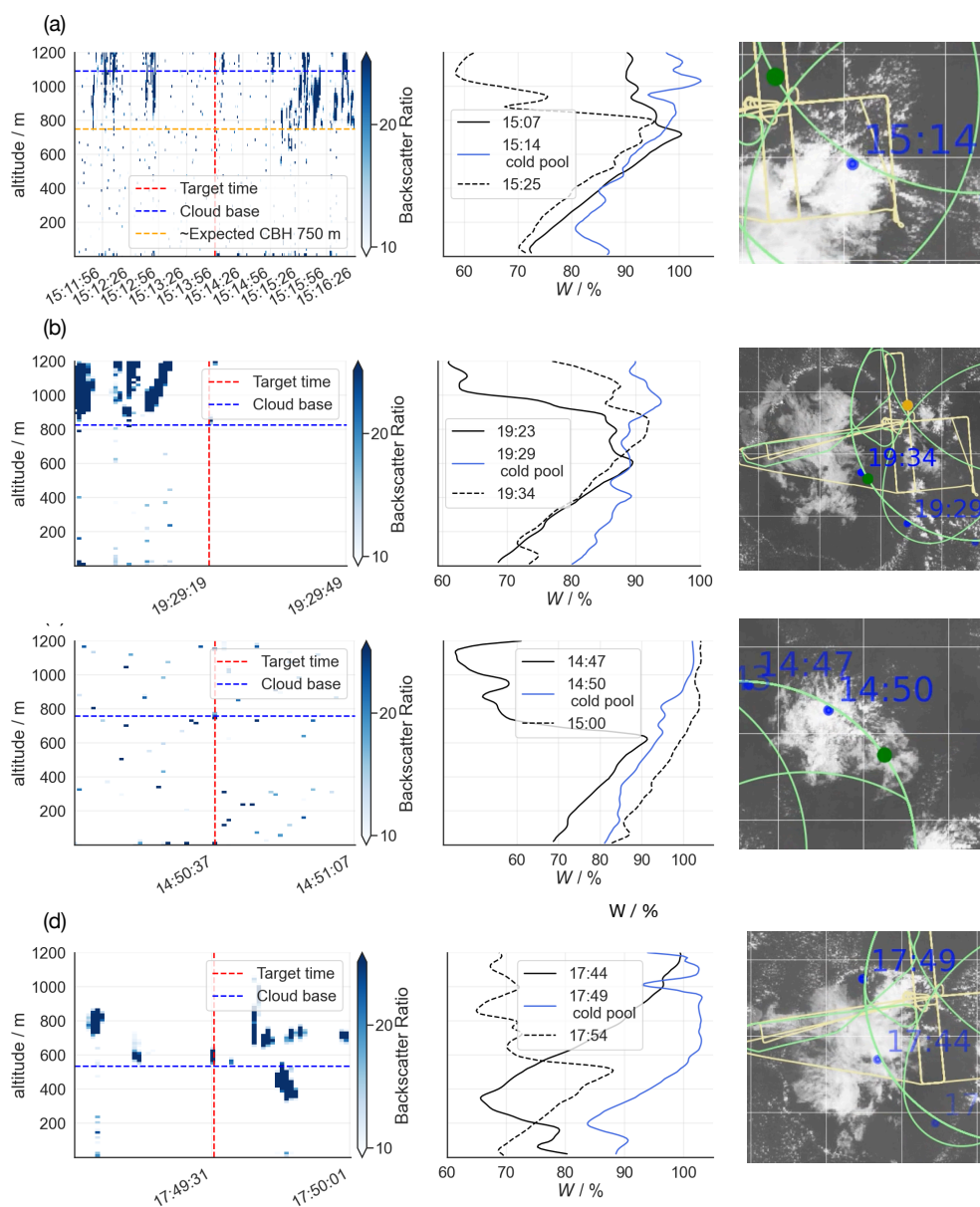
Figure 6. The four anomalous W_a and h pairings labeled as outliers, (a), (b), (c), and (d), in Fig. 5. Left column: the backscatter ratio including the selected time as vertical line (red), the inferred cloud base height (blue horizontal line), and for the top panel, an approximate cloud base height value expected from the linear relationship (orange horizontal line); center column: relative humidity profiles for the nearest sounding in blue, as well as the soundings immediately before and after (black, solid and dashed, respectively); right column: visible satellite images (GOES-16 ABI) illustrating the cloud organization from above and the location of the dropsonde at its launch time, accessed via https://observations.ipsl.fr/aeris/eurec4a-data/PRODUCTS/GOES-E_movies/VIS_IR_combined/v1.0.0/.

11

of relative humidity for the closest dropsonde and the dropsondes immediately prior and after, and visible satellite images of the cloud formations (Fig. 6). A visual inspection of the scenes around the anomalous points suggest that the outliers are associated

215 with cold pools that increase relative humidity (increasing specific humidity and decreasing temperature) (Touzé-Peiffer et al., 2022), and/or cloud fragments associated with dissipating or stratiform cloud elements. The outlier labeled (a) appears to be a cloud fragment from the stratiform cloud layer, as seen in the backscatter ratios and, to some extent, in the visible satellite image; it is associated with higher relative humidity than the dropsonde sounding immediately before and after. If instead estimating a cloud base height around 750 m and relative humidity between 70–75% representative of the larger environment,

220 the point would align with the other data, as illustrated schematically in Fig. 5. Cases (b) and (c) correctly identify the cloud base height, but the cold pool soundings have higher-than-expected relative humidity as seen in the dropsonde profiles. This high value of W_a result in a $W_a(h)$ relationship that differs from the expected linear relationship, but these values would not be expected to be associated with significant errors in the inferred relative humidity because the cloud base height estimate is not biased. Having removed these outliers on Feb. 2, the WALES lidar method has similar skill to ground-based lidar estimates

225 as shown in Fig. 4.

In addition, point (d) in the figure appears to be associated with cloud forming on a cold pool boundary, which was uncharacteristic of the broader cloud environment (Fig. 6d). Here again it appears that the value does not violate the $W_a(h)$ relationship used to estimate W_a from h, but rather violates the correspondence between the humidity estimate and the lidar selection of the lowest cloud base. Recalculating the correlation with a cloud base height value of 300 m, the association increases (to r =

230 -0.86). This example suggests some ambiguity in the estimate of W_a based on the spread of cloud base estimates below the peak value of the distribution, something that would have to be fine-tuned in an operational retrieval.

4.3 Estimates of $\frac{\mathrm{d}W}{\mathrm{d}z}$ and $\Delta_a T$

To operationalize our framework requires estimating the two near-surface control parameters, $\frac{\mathrm{d}W}{\mathrm{d}z}$ and $\Delta_a T$, from observations and adopt representative values to convert $W_a(z_a)$ into $q_s - q_a$ in the analysis. To test the proposed method we use the EUREC[4]A

235 data. If these ideas were used to develop an operational product, they may need to be tuned, perhaps to depend on ambient conditions from a prior expectation or other product.

Figure 7 shows the distribution of relative-humidity lapse rates, $\frac{\mathrm{d}W}{\mathrm{d}z}$, calculated from R/V *Meteor* radiosondes launched between 16 January and 1 March 2020. Soundings are separated into cloudy profiles (where W reaches 100% below 1 km) and non-cloudy profiles. The lapse rate is estimated from a linear regression between 200 and 400 m. For cloudy soundings, which

240 occur about 10% of the time, the mean is $3.9\,\%\,\mathrm{hm}^{-1}$ (median $3.8\,\%\,\mathrm{hm}^{-1}$; 5–95% range $2.4\,\%\,\mathrm{hm}^{-1}$ to $4.7\,\%\,\mathrm{hm}^{-1}$). For non-cloudy soundings, the distribution is broader with a median of $3.5\,\%\,\mathrm{hm}^{-1}$ (5–95% range $1.1\,\%\,\mathrm{hm}^{-1}$ to $4.9\,\%\,\mathrm{hm}^{-1}$).

These empirical estimates agree closely with the theoretical expectations derived in Sec. 3, where Eq. (3) predicted an adiabatic rate of $\frac{\mathrm{d}W}{\mathrm{d}z} \approx 4.0\,\%\,\mathrm{hm}^{-1}$ and Eq. (4) gave a slightly smaller non–well-mixed value of about $3.3\,\%\,\mathrm{hm}^{-1}$. Based on these results, in the subsequent analysis, we adopt $\frac{\mathrm{d}W}{\mathrm{d}z} = 4\,\%\,\mathrm{hm}^{-1}$ as a representative value—close to both the peak of the

245 cloudy-sounding distribution and the theoretical estimate.
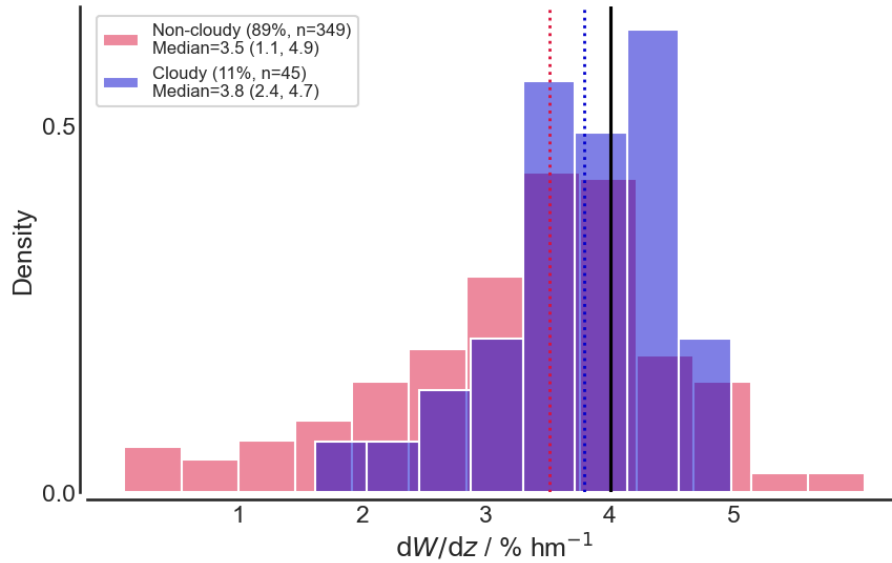
Figure 7. Histograms of $\frac{dW}{dz}$ calculated from R/V Meteor soundings as a linear regression between $200\,\mathrm{m}$ to $400\,\mathrm{m}$: cloudy soundings (blue), defined as soundings where $W \geq 100\%$ below $1\,\mathrm{km}$, and non-cloudy soundings (red) otherwise. Vertical dashed lines mark the median of each distribution, and the solid black line marks the representative value of $4\,\%\,\mathrm{hm}^{-1}$ used in the analysis.

For $z_a = 40\,\mathrm{m}$, $\delta_{\mathrm{a}}P$ is negligible compared with P. Given W_{a}, we can therefore calculate $q_{\mathrm{s}} - q_{\mathrm{a}}$ from $h\frac{dW}{dz}$ and $\Delta_a T$. Because both $\frac{dW}{dz}$ and $\Delta_a T$ are controlled by boundary-layer dynamics and the near-adiabatic temperature structure, both quantities are expected to remain relatively constant over time.

Figure 8a shows the time evolution of sea-surface temperatures measured by the port thermosalinograph (depth $5\,\mathrm{m}$) and near-surface air temperatures measured at $28.3\,\mathrm{m}$. The seawater measurements are expected to be biased warm relative to the true skin temperature due to the cool-skin effect, typically $0.1\,\mathrm{K}$ to $0.3\,\mathrm{K}$ (Fairall et al., 1996a; Yan et al., 2024). As expected, nearly all (97%) of the 47,512 measurements show the ocean warmer than the overlying air, consistent with unstable and convective conditions. The median and mean temperature differences are 1.0 and $1.1\,\mathrm{K}$, respectively. Because the relevant temperature for surface fluxes is the sea-surface *skin* temperature, we take it to be $0.3\,\mathrm{K}$ cooler than the measured bulk temperature, yielding a representative offset of $\Delta_a T = 1.3\,\mathrm{K}$. This fixed offset is applied to the sea-surface temperatures corresponding to each radiosonde launch.

4.4 Retrieval skill in q_a

We now evaluate the retrieval skill of the cloud base-height method for near-surface specific humidity, q_a, by comparing predicted values with co-located sounding observations. Fig. 9a,b presents the time series of predicted near-surface specific humidity, q_a, based on 171 co-located ceilometer–radiosonde pairs and observed radiosondes launched from the R/V Meteor. On average the cloud base height method overestimates q_a by $0.33\,\mathrm{g\,kg}^{-1}$ (5th–95th percentile range: $-0.74\,\mathrm{g\,kg}^{-1}$ to $1.8\,\mathrm{g\,kg}^{-1}$),
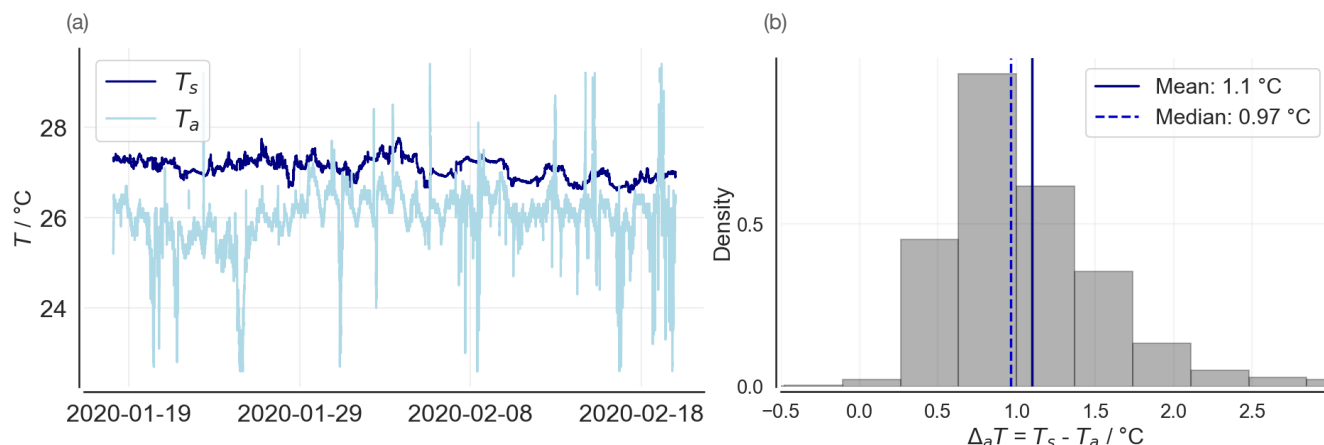
Figure 8. (a) Time series of sea-surface temperatures (T_s), measured 5 m below the ocean surface, and near-surface air temperatures (T_a), measured at 28.3 m on the R/V *Meteor*. (b) Distribution of temperature differences, $\Delta_a T = T_s - T_a$, with vertical lines for the mean and median values.

with a median absolute error of $0.47\,\mathrm{g\,kg^{-1}}$. The temporal variability is well captured ($r = 0.76$). The largest positive biases occur early in the campaign when cloud bases were low – the error in q_a correlates with cloud-base height ($r = 0.54$ overall, rising to $r = 0.76$ for bases below 600 m), suggesting that shallow, poorly mixed layers (e.g., beneath decaying cold pools; see

265   Fig. 6) are less amenable to this approximation. No systematic diurnal bias is evident, although the small sample size limits a definitive assessment of hour-of-day effects.

Figure 9c,d shows the comparison between WALES airborne lidar–derived q_a estimates and coincident dropsonde measurements also from HALO. Here the cloud-base method again reproduces the variability reasonably well ($r = 0.61$), with a small mean bias of $-0.06\,\mathrm{g\,kg^{-1}}$ and a median absolute error of $0.26\,\mathrm{g\,kg^{-1}}$ on January 28, 2020. On February 2, 2020, the

270   correlation is slightly lower ($r = 0.57$), with a mean bias of $-0.03\,\mathrm{g\,kg^{-1}}$ and a median absolute error of $0.27\,\mathrm{g\,kg^{-1}}$.

5   Scope, caveats, and practical use

The method proposed in this study is designed for convective marine boundary layers in which the subcloud layer is well mixed and shallow cumulus clouds are coupled to the surface. These conditions are ubiquitous over the world ocean (Fig.1). In such conditions, the cloud base height corresponds closely to the lifting condensation level, which depends primarily on the

275   near-surface temperature and humidity.

Despite the ubiquity of favorable conditions, several processes can violate the proxy's assumptions or introduce measurement bias. Cold pools from downdrafts and rain-driven outflows can produce shallow, moist layers decoupled from the overlying cloud, lowering the observed cloud base relative to the environmental LCL and thus overestimating q_a. Optically thick or
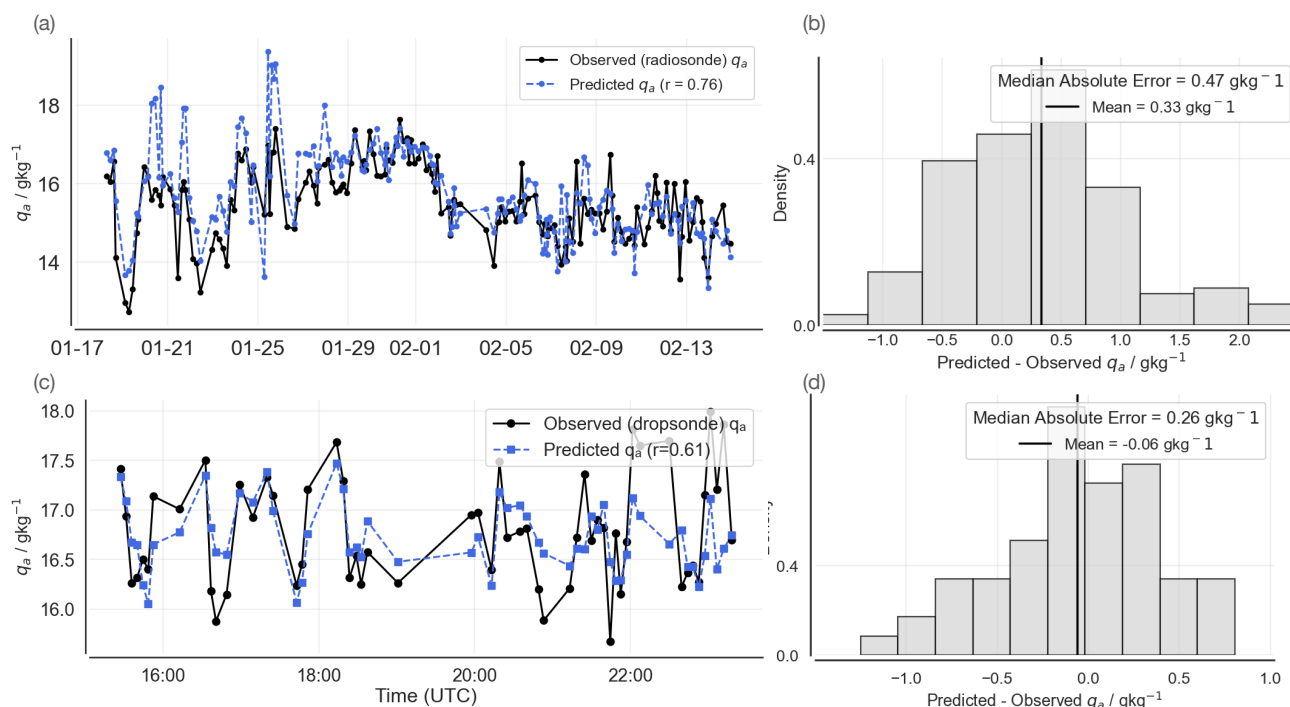
Figure 9. Comparison of observed and predicted near-surface specific humidity estimates and their error distributions. (a) Time series of observed q_a from radiosondes launched from the R/V Meteor (solid black) versus the cloud base-height-derived prediction from R/V Meteor ceilometer data (dashed blue; $r = 0.76$). Time is month and day. (b) Histogram of predicted minus observed q_a for the R/V Meteor data with a median absolute error of $0.47\,\mathrm{g\,kg^{-1}}$ and a mean bias of $0.33\,\mathrm{g\,kg^{-1}}$ (vertical line). (c) Time series of observed q_a from HALO dropsondes (solid black) versus cloud base-height-derived predictions from WALES airborne lidar estimates on January 28, 2020 (dashed blue, $r = 0.64$). Time is hour and minute, UTC. (d) Histogram of predicted minus observed q_a for the HALO comparison, with a median absolute error of $0.26\,\mathrm{g\,kg^{-1}}$ and a mean bias of $-0.06\,\mathrm{g\,kg^{-1}}$ (vertical line).

multilayer clouds pose observational limits: a lidar or ceilometer may detect an upper cloud base rather than the lowest, inflating
280 the apparent cloud base height and biasing the inferred near-surface humidity low; optical-depth and multilayer screening are therefore required. Shallow or weakly mixed layers, in addition to those induced by cold pools, depart from the well-mixed assumption, weakening the cloud base and surface-humidity link and typically yielding low-biased estimates of q_{a} unless filtered.

Accordingly, the proxy should be applied only where boundary-layer conditions are convective and the detected cloud base
285 is the lowest layer coupled to the surface. These conditions can be diagnosed using coincident lidar backscatter, optical-depth screening, or reanalysis-based buoyancy metrics as in Fig. 1. Within such convective marine regimes, the method's assumptions hold and the resulting estimates of near-surface specific humidity are expected to be reliable.

6   Discussion and conclusions

We show that downward-looking lidar retrievals of cloud base height can be used to infer near-surface relative humidity.
290   Combined with wind speed, sea surface temperature, and the near-surface air–sea temperature difference, this information
enables physically-based estimates of the surface water vapor flux. Over the ocean, where such measurements are both scarce
and essential for the surface energy balance, scatterometers provide wind speed, and long-running satellite records provide
sea-surface temperature. Because the air–sea temperature difference varies only modestly across most of the global ocean, it
can be estimated statistically. Thus, relative humidity inferred from cloud base height supplies a key missing ingredient for
295   remote-sensing estimates of the surface water vapor flux.

The method we propose for estimating near-surface humidity requires unbiased estimates of cloud base height, and the
satisfaction of two further assumptions: (i) that the relative humidity lapse rate is near the value it would obtain in a well-mixed
layer, and thus relatively constant; and (ii) that the near-surface air temperature is cooler than the surface, so that the layer above
is convectively driven. Convective boundary layer clouds – which form in the radiatively cooled, cold advection-dominated
300   boundary layers that prevail over tropical oceans – both underpin our near-surface humidity estimates and confirm that the
very conditions required for those estimates are in place. While this physical situation limits the application of the method to
conditions where shallow convective clouds are present, they are ubiquitous, even in regions of deep convection. Our analysis
shows that the method will benefit from some calibration for estimating cloud base from a distribution of lidar echoes, for
estimating the relative humidity lapse rate, and for estimating the air-sea temperature difference. Their unbiased estimation
305   will be required for using the proposed method to establish large-scale climatologies of near-surface relative humidity and
associated moisture fluxes.

As an outlook we note that the method we propose could facilitate the development of a long-term, day and night, and
physically-based near-surface humidity climatology if applied to global data of cloud base height. Techniques using multi-
angle satellite imagery have been shown to retrieve cloud base height, albeit over longer timescales (Böhm et al., 2019). The
310   most promising candidate for obtaining such data is measurements using a spaceborne lidar. Currently the newly-launched
EarthCARE satellite (Illingworth et al., 2015) provides HSR-Lidar data. It provides backscatter data with a horizontal reso-
lution of about $280 \, \mathrm{m}$ and a vertical resolution of $100 \, \mathrm{m}$. While the horizontal resolution appears to be sufficient to apply our
method, the limited vertical resolution would imply an error of the near-surface humidity of about $0.5 \, \mathrm{g \, kg^{-1}}$ attributed to the
vertical sampling error alone (based on Eq. (9) assuming typical values for W_a, h, etc.). With sufficient sampling, and given the
315   variability of cloud base height, it might be possible to obtain greater precision in estimates of the mean cloud base height than
what is implied by the single-snapshot vertical resolution. Laser ranging using more sophisticated methods, such as employed
by the Global Ecosystem Dynamics Investigation lidar aboard the International Space Station, could provide better estimates
of cloud base height. But presently GEDI does not provide data products that allow this capability to be explored. Future
satellites refining these technologies could be adapted to the conditions of the proposed method, and potentially could provide
320   coincident estimates of near-surface wind speed and air-sea temperature difference. In this context, measurements of ocean
surface texture using synthetic aperture radar could also be explored as a way to estimate the difference between the surface

temperature and that of the air just above it, which would better constrain the proposed estimates both directly, and indirectly due to the expected covariability of the relative humidity lapse rate and the air-sea temperature difference. At the least, our work suggests that cloud base height information from lidar measurements could be usefully incorporated into reanalyses and into

325 existing statistical flux retrieval frameworks – such as those used in HOAPS, SeaFlux, IFREMER, or J-OFURO climatologies (e.g., Gentemann et al., 2020; Liman et al., 2018; Bentamy et al., 2017a; Tomita et al., 2019) – to better constrain near-surface humidity and surface moisture fluxes.

References

335   Albright, A. L., Bony, S., Stevens, B., and Vogel, R.: Observed subcloud layer moisture and heat budgets in the trades, Journal of the Atmospheric Sciences, 79, 2363–2385, 2022.

Andersson, A., Fennig, K., Klepp, C., Bakan, S., Graßl, H., and Schulz, J.: The Hamburg ocean atmosphere parameters and fluxes from satellite data–HOAPS-3, Earth System Science Data, 2, 215–234, 2010.

Bentamy, A., Grodsky, S. A., Katsaros, K., Mestas-Nuñez, A. M., Blanke, B., and Desbiolles, F.: Improvement in air–sea flux estimates

340   derived from satellite observations, International Journal of Remote Sensing, 34, 5243–5261, 2013.

Bentamy, A., Grodsky, S. A., Elyouncha, A., Chapron, B., and Desbiolles, F.: Homogenization of scatterometer wind retrievals, International Journal of Climatology, 37, 870–889, 2017a.

Bentamy, A., Piolle, J.-F., Grouazel, A., Danielson, R., Gulev, S., Paul, F., Azelmat, H., Mathieu, P., von Schuckmann, K., Sathyendranath, S., et al.: Review and assessment of latent and sensible heat flux accuracy over the global oceans, Remote Sensing of Environment, 201,

345   196–218, 2017b.

Böhm, C., Sourdeval, O., Mülmenstädt, J., Quaas, J., and Crewell, S.: Cloud base height retrieval from multi-angle satellite data, Atmospheric Measurement Techniques, 12, 1841–1860, 2019.

Bony, S., Stevens, B., Ament, F., Bigorre, S., Chazette, P., Crewell, S., Delanoë, J., Emanuel, K., Farrell, D., Flamant, C., et al.: EUREC4A: A field campaign to elucidate the couplings between clouds, convection and circulation, Surveys in Geophysics, 38, 1529–1568, 2017.

350   Bony, S., Schulz, H., Vial, J., and Stevens, B.: Sugar, gravel, fish, and flowers: Dependence of mesoscale patterns of trade-wind clouds on environmental conditions, Geophysical research letters, 47, e2019GL085 988, 2020.

Bourras, D.: Comparison of five satellite-derived latent heat flux products to moored buoy data, Journal of Climate, 19, 6291–6313, 2006.

Clayson, C. and Brown, J.: NOAA Climate Data Record Ocean Surface Bundle (OSB) Climate Data Record (CDR) of Ocean Heat Fluxes, Version 2, Clim. Algorithm Theor. Basis Doc. C-ATBD Asheville NC NOAA Natl. Cent. Environ. Inf. Doi, 10, V59K4885, 2016.

355   Clayson, C., Rutgersson, A., Ward, B., de Souze, R., Edson, J., Gleckler, P., Heil, P., Ichii, K., Jung, M., Miralles, D., et al.: WCRP Surface Flux Task Team—A White Paper Outlining the Need for a Coordinated High-Level Approach to Improving Our Understanding of Surface-Atmosphere Fluxes, World Climate Research Programme: Geneva, Switzerland, 2019.

Edson, J. B., Jampana, V., Weller, R. A., Bigorre, S. P., Plueddemann, A. J., Fairall, C. W., Miller, S. D., Mahrt, L., Vickers, D., and Hersbach, H.: On the exchange of momentum over the open ocean, Journal of Physical Oceanography, 43, 1589–1610, 2013.

360   Esselborn, M., Wirth, M., Fix, A., Tesche, M., and Ehret, G.: Airborne high spectral resolution lidar for measuring aerosol extinction and backscatter coefficients, Appl. Opt., 47, 346–358, https://doi.org/10.1364/AO.47.000346, 2008.

Fairall, C. W., Bradley, E. F., Godfrey, J. S., Wick, G. A., Edson, J. B., and Young, G. S.: Cool-skin and warm-layer effects on sea surface temperature, Journal of Geophysical Research: Oceans, 101, 1295–1308, https://doi.org/10.1029/95JC03190, 1996a.

Fairall, C. W., Bradley, E. F., Rogers, D. P., Edson, J. B., and Young, G. S.: Bulk parameterization of air-sea fluxes for tropical ocean-global

365   atmosphere coupled-ocean atmosphere response experiment, Journal of Geophysical Research: Oceans, 101, 3747–3764, 1996b.

Fairall, C. W., Bradley, E. F., Hare, J., Grachev, A. A., and Edson, J. B.: Bulk parameterization of air–sea fluxes: Updates and verification for the COARE algorithm, Journal of climate, 16, 571–591, 2003.

Fajber, R., Donohoe, A., Ragen, S., Armour, K. C., and Kushner, P. J.: Atmospheric heat transport is governed by meridional gradients in surface evaporation in modern-day earth-like climates, Proceedings of the National Academy of Sciences, 120, e2217202 120, 2023.

370 Gentemann, C. L., Clayson, C. A., Brown, S., Lee, T., Parfitt, R., Farrar, J. T., Bourassa, M., Minnett, P. J., Seo, H., Gille, S. T., et al.: FluxSat: measuring the ocean–atmosphere turbulent exchange of heat and moisture from space, Remote Sensing, 12, 1796, 2020.

George, G., Stevens, B., Bony, S., Pincus, R., Fairall, C., Schulz, H., Kölling, T., Kalen, Q. T., Klingebiel, M., Konow, H., et al.: JOANNE: Joint dropsonde Observations of the Atmosphere in tropical North atlaNtic meso-scale Environments, Earth System Science Data, 13, 5253–5272, 2021.

375 Hartmann, D. L.: Global physical climatology, vol. 103, Newnes, 2015.

Illingworth, A. J., Barker, H., Beljaars, A., Ceccaldi, M., Chepfer, H., Clerbaux, N., Cole, J., Delanoë, J., Domenech, C., Donovan, D. P., et al.: The EarthCARE satellite: The next step forward in global measurements of clouds, aerosols, precipitation, and radiation, Bulletin of the American Meteorological Society, 96, 1311–1332, 2015.

Jackson, D. L., Wick, G. A., and Robertson, F. R.: Improved multisensor approach to satellite-retrieved near-surface specific humidity

380 observations, Journal of Geophysical Research: Atmospheres, 114, 2009.

Konow, H., Ewald, F., George, G., Jacob, M., Klingebiel, M., Kölling, T., Luebke, A. E., Mieslinger, T., Pörtge, V., Radtke, J., et al.: EUREC4A's HALO, Earth System Science Data, 13, 5545–5563, 2021.

Kubota, M. and Tsutomu, H.: Retrieval of surface air specific humidity over the ocean using AMSR-E measurements, Sensors, 8, 8016–8026, 2008.

385 Liman, J., Schröder, M., Fennig, K., Andersson, A., and Hollmann, R.: Uncertainty characterization of HOAPS 3.3 latent heat-flux-related parameters, Atmospheric Measurement Techniques, 11, 1793–1815, 2018.

Nuijens, L., Serikov, I., Hirsch, L., Lonitz, K., and Stevens, B.: The distribution and variability of low-level cloud in the North Atlantic trades, Quarterly Journal of the Royal Meteorological Society, 140, 2364–2374, 2014.

Oliver, J. E.: Bowen Ratio, in: Encyclopedia of World Climatology, edited by Oliver, J. E., pp. 133–135, Springer, Dordrecht, ISBN 978-1-

390 4020-3266-0, https://doi.org/10.1007/0-387-30749-4_30, 2005.

Ricciardulli, L. and Manaster, A.: Intercalibration of ASCAT scatterometer winds from MetOp-A,-B, and-C, for a stable climate data record, Remote Sensing, 13, 3678, 2021.

Roberts, J. B., Clayson, C., and Robertson, F.: Improving near-surface retrievals of surface humidity over the global open oceans from passive microwave observations, Earth and Space Science, 6, 1220–1233, 2019.

395 Robertson, F. R., Roberts, J. B., Bosilovich, M. G., Bentamy, A., Clayson, C. A., Fennig, K., Schröder, M., Tomita, H., Compo, G. P., Gutenstein, M., et al.: Uncertainties in ocean latent heat flux variations over recent decades in satellite-based estimates and reduced observation reanalyses, Journal of Climate, 33, 8415–8437, 2020.

Stephan, C. C., Schnitt, S., Schulz, H., Bellenger, H., De Szoeke, S. P., Acquistapace, C., Baier, K., Dauhut, T., Laxenaire, R., Morfa-Avalos, Y., et al.: Ship-and island-based atmospheric soundings from the 2020 EUREC4A field campaign, Earth System Science Data Discussions,

400 2020, 1–35, 2020.

Stevens, B., Farrell, D., Hirsch, L., Jansen, F., Nuijens, L., Serikov, I., Brügmann, B., Forde, M., Linne, H., Lonitz, K., et al.: The Barbados Cloud Observatory: Anchoring investigations of clouds and circulation on the edge of the ITCZ, Bulletin of the American Meteorological Society, 97, 787–801, 2016.

Stevens, B., Bony, S., Brogniez, H., Hentgen, L., Hohenegger, C., Kiemle, C., L'Ecuyer, T. S., Naumann, A. K., Schulz, H., Siebesma, P. A.,

405 et al.: Sugar, gravel, fish and flowers: Mesoscale cloud patterns in the trade winds, Quarterly Journal of the Royal Meteorological Society, 146, 141–152, 2020.

Stevens, B., Bony, S., Farrell, D., Ament, F., Blyth, A., Fairall, C., Karstensen, J., Quinn, P. K., Speich, S., Acquistapace, C., et al.: EUREC4A, Earth System Science Data Discussions, 2021, 1–78, 2021.

Tomita, H. and Kubota, M.: An analysis of the accuracy of Japanese Ocean Flux data sets with Use of Remote sensing Observations (J-OFURO) satellite-derived latent heat flux using moored buoy data, Journal of Geophysical Research: Oceans, 111, 2006.

Tomita, H., Hihara, T., Kako, S., Kubota, M., and Kutsuwada, K.: An introduction to J-OFURO3, a third-generation Japanese ocean flux data set using remote-sensing observations, Journal of Oceanography, 75, 171–194, 2019.

Touzé-Peiffer, L., Vogel, R., and Rochetin, N.: Cold pools observed during EUREC4A: Detection and characterization from atmospheric soundings, Journal of Applied Meteorology and Climatology, 61, 593–610, 2022.

Vaisala: Vaisala Radiosonde RD41 datasheet in English, B211706EN-B, Tech. rep., Vaisala, available at: https://www.vaisala.com/sites/default/files/documents/RD41-Datasheet-B211706EN.pdf (last access: 9 November 2021), 2020.

Vogel, R., Albright, A. L., Vial, J., George, G., Stevens, B., and Bony, S.: Strong cloud–circulation coupling explains weak trade cumulus feedback, Nature, pp. 1–5, 2022.

Wirth, M., Fix, A., Mahnke, P., Schwarzer, H., Schrandt, F., and Ehret, G.: The airborne multi-wavelength water vapor differential absorption lidar WALES: system design and performance, Applied Physics B, 96, 201, https://doi.org/10.1007/s00340-009-3365-7, 2009.

Wyngaard, J. C. and Brost, R. A.: Top-down and bottom-up diffusion of a scalar in the convective boundary layer, Journal of Atmospheric Sciences, 41, 102–112, 1984.

Yan, Y., Song, X., Wang, G., and Li, X.: Tropical Cool-Skin and Warm-Layer Effects and Their Impact on Surface Heat Fluxes, Journal of Physical Oceanography, 54, 45–62, https://doi.org/10.1175/JPO-D-23-0103.1, 2024.